



Contents lists available at ScienceDirect

Corrosion Science

journal homepage: www.elsevier.com/locate/corsci

Interfacial layer on archaeological mild steel corroded in carbonated anoxic environments studied with coupled micro and nano probes

Y. Leon^a, M. Saheb^b, E. Drouet^a, D. Neff^a, E. Foy^a, E. Leroy^c, J.J. Dynes^d, P. Dillmann^{a,*}

^a LAPA: NIMBE, SIS2M UMR3299 CEA/CNRS and IRAMAT UMR5060 CNRS, CEA Saclay, 91191 Gif sur Yvette Cedex, France

^b LISA: UMR CNRS 7583, Université Paris-Est Créteil and Université Paris-Diderot, 61 avenue du Général de Gaulle, 94010 Créteil Cedex, France

^c ICMPE: UMR 7182 CNRS/UPEC, 2 rue Henri Dunant, 94320 Thiais, France

^d Canadian Light Source, 44 Innovation Boulevard, Saskatoon, SK S7N 2V3, Canada

ARTICLE INFO

Article history:

Received 7 March 2014

Accepted 6 July 2014

Available online xxxx

Keywords:

A. Carbon steel

C. Interfaces

B. AFS (EXAFS & XANES)

B. TEM

B. Raman spectroscopy

ABSTRACT

The interfacial layer formed on archaeological artefacts corroded during 450 years in carbonated anoxic water was studied using FEG–SEM, Raman, STEM, STXM. This layers forms between the metallic substrate and an outer carbonate layer. Interfacial layer shows various thicknesses from about 100 nm to several μm . It is made of a mix of iron oxides (maghemite or magnetite). A formation mechanism is proposed and based on slight pH increase at the interface. D₂O labelling experiments show that the penetration of water in the pore network seems to be significantly hindered at the interface by the presence of the oxide layers.

© 2014 Elsevier Ltd. All rights reserved.

1. Introduction

The anoxic corrosion of mild steel in carbonated environments is a major issue [1], for diverse structures such as pipelines used for oil and gas transport [2,3], steel canisters proposed for use in the deep storage of nuclear wastes in several countries [4,5] or for the *in situ* conservation of archaeological iron artefacts [6,7]. In addition to their interest for conservation purposes, studies of archaeological iron artefacts, recovered from these environments, help to predict the corrosion of mild steels over long time periods [8,9]. Some differences could exist between the different systems concerning the nature of the materials and the environment but the information provided by studies on archaeological analogues on phases and system formed after several centuries are of primary interest to identify dimensioning mechanisms and calibrate models [9,10]. Moreover in many cases it is possible to select sites and samples the closest as possible to the system of interest. For example samples presenting comparable microstructure with the contemporary mild steels can be selected (e.g., without any segregation of minor elements or with a low content of second phase particles as slag inclusions [11]). Saheb et al. [12–14] studied archaeological nails coming from the Glinet and Nydam Mose sites (these sites are studied for several years and representative of anoxic carbonated soils) at the micrometre scale and showed that

the main corrosion products were mainly iron carbonates such as siderite (FeCO_3) and chukanovite ($\text{Fe}_2(\text{OH})_2\text{CO}_3$), occurring as layers around the metal (total thickness several 100 μm), the latter located closest to the metal. In addition to these products, an external layer of magnetite (Fe_3O_4) was sometimes observed. This layer corresponds to the remaining phases of a former mill scale initially present on the artefact before its burial. Moreover, some isolated areas of several 10 μm , made of magnetite (sometimes mixed with maghemite $\gamma\text{-Fe}_2\text{O}_3$) could be found locally in the siderite layer, sometimes in contact with the metal. Recent studies on an archaeological nail using X-ray absorption spectroscopy (XAS) implemented in scanning transmission X-ray microscopy (STXM) suggest that an interfacial layer consisting of a mixture of magnetite and maghemite, several 100 nm thick, could grow between the metal and carbonate layer [15]. Unfortunately this preliminary study was limited to a single sample and was only investigated by STXM. Thus, up to now, very few data have been collected on that layer.

In a parallel way, several studies performed in comparable conditions on shorter times on laboratory samples also suggest the presence of a passivating (multi)layer [16] or mixture [17] on the tested samples. Some other studies suggest that this interface is made of a nanometre scale made of oxides (maghemite and magnetite) that could control the corrosion kinetics and potentially passivate the metal. This layer was found by Bataillon et al. [18] in experiments aiming to reconstitute the condition of deep nuclear waste storage in clay saturated with water, but also by

* Corresponding author.

E-mail address: philippe.dillmann@cea.fr (P. Dillmann).

authors studying corrosion in aqueous CO₂ environments [19]. The same kind of interfacial layer was also found on iron corroded in anaerobic borate buffer solutions (neutral or slightly alkaline pH). A spinel oxide layer intermediate between magnetite and maghemite was found by XRD synchrotron experiment or XPS [20–22]. Lastly, Lee et al [23,24], observed after several 10 h of corrosion of mild steel, depending on the carbonate concentration of the deaerated neutral solution, the occurrence of porous siderite (in concentrated carbonate solution) and a mix of siderite, carbonated green rust (4Fe(OH)₂·2Fe(OH)₃CO₃) and magnetite for lower carbonate concentration. Unfortunately, these authors do not study precisely the location of the different layers in the corrosion system. Other studies suggested that Fe(OH)₂ and FeCO₃ initially formed on the steel oxidize to γ -Fe₂O₃, Fe₃O₄, and other Fe³⁺ oxides under certain conditions [25,26].

To better understand the corrosion mechanisms involved in archaeological systems on very long term and the potential role of an interfacial layer on kinetic control during long periods of corrosion, the present study aims to develop systematic observations at nanoscale on a set of several archaeological artefacts by a step to step multi-scale characterisation approach (coupling SEM–FEG, μ Raman spectroscopy, MET, STXM implementing XAS observations at Fe and C K edges). Moreover the transport properties of the interfacial layer were also investigated by D₂O tracing coupled with nanoSIMS detection. The aim is here to bring more data on the nature of the interfacial layer in order to understand its formation and its role in the corrosion mechanisms.

2. Set of samples

Four 450 years-old nails (GL10-01, GL10-03, GL10-04 and GL07-40) were excavated from the archaeological site of Glinet (Seine Maritime, France). The metal in the nails was a mild steel with a C content ranging from lower than 0.02–0.1% [12]. They come from a zone, about 1 m below surface, where the pores of the soil are saturated with an anoxic calcium-bicarbonate water ($4 \cdot 10^{-3} \text{ mol L}^{-1} < \text{TIC} < 1 \cdot 10^{-2} \text{ mol L}^{-1}$) at neutral pH (6.9–7.4) [14]. Anoxic conditions were carefully preserved by using sealed packaging under N₂ (O₂ concentration < 100 ppm) from the excavation to the analyses and during the sample preparation. Nevertheless this procedure could not allow one to avoid a very short exposure to air between the excavation and the bag sealing (less than 1 min).

3. Methods

A transverse section of each nail was prepared in a glove box under N₂ atmosphere by classical grinding and polishing (3 and 1 μm diamond paste) under ethanol (for more details see [27,28]). A homemade cell allowed us to bring the sample to Field Emission Gun–Scanning Electron Microscope (FEG–SEM), micro Raman Spectrometer (μRS) and other sample preparation devices without any contact with oxygen.

Observation and composition studies have been carried out with an Energy Dispersive X-ray EDX system coupled to a FEG–SEM (JEOL SEM 7001F). The system allows for high-resolution up to 10 nm. Samples were observed in backscattered electron mode. Analyses were performed with a 15 kV accelerating voltage and with a probe current of about 20 nA. The EDX system is a SAMx microanalysis application software coupled with a Silicon Drift Detector (SDD) from SGX SENSORTECH company. This system permits high-count rates (about 100 Kcps/s) with good spectral resolution (130 eV on Mn K-alpha). X-ray mapping (512 \times 382 pixels) was carried out with MaxView imaging software provided by the

SAMx+ society after selection an energy ROI for each element of interest on the EDS spectrum.

Micro-Raman measurements were performed by means of an Invia reflex spectrometer from Renishaw®. It is equipped with a frequency-doubled Nd: YAG laser emitting at 532 nm and with a charge-coupled device multichannel matrix CCD detector cooled by Peltier effect. A 50 \times optical microscope LEICA objective was employed to focus the laser beam and to collect the scattered light, providing a laser spot size on the samples less than 2 μm . A 2400 l/mm grating induces a spectral resolution of about 1 cm^{-1} . The laser beam power on the surface of the sample can be modulated through optical density filters to optimize the signal/background ratio and to avoid the thermal modification of the analysed iron corrosion products; we chose to record the spectra with a laser power of about 100 μW on the sample. It was verified that, at this very low power, no phase transformation occurs under the laser beam. Wavenumber calibration was regularly verified by using the Raman peak at 520 cm^{-1} of a silicon crystal as a reference and phases were identified by comparison with spectra obtained on synthesized powders and found in the literature (Tables 1 and 2). Maps are collected thanks to a motorized stage. The data processing delivering qualitative information about the main phase present at each pixel is conducted following a usual method based on the selection of the cumulated signal in a Region of Interest (ROI) corresponding to a wavenumber range characteristic of the main peak of each considered phase (see Tables 1 and 2). Maps plots the intensity of the collected signal in the ROI corrected by a baseline linearly modelled [29]. All characterisations were realised in a home made cell allowing to acquire Raman spectra on the sample kept in anoxic atmosphere through a 1 mm thick BK7 window (see Fig. 1).

Complementary to FEG–SEM observations, in order to investigate the samples at nanoscales, two methods were implemented: Transmission Electron Microscopy (TEM) and Scanning Transmission X ray Microscopy (STXM). To that purpose, thin films were taken at representative places of the transverse sections at the metal–corrosion layer interface. Milling was performed with a FEI Strata 235 Dual Beam focused ion beam (FIB) system. The *in situ* lift-out technique allows the sample to be fixed to a TEM-grid inside the Dual beam Instrument without exposure to the atmosphere. A thin film with an 80 nm thickness was obtained.

The low-resolution imaging and electron diffraction investigations were carried out with a FEI Tecnai F20 electron microscope. It is equipped with an objective lens Super Twin, a 200 kV field emission gun (FEG) and a scanning image observation device (STEM) with a set of STEM detectors (Bright Field, Annular Dark Field and High Angle Angular Dark Field). Its resolution is approximately 2.4 Å. This microscope chamber is also equipped with a cold finger system, which is essential for preserving sensitive samples. Samples were analysed at an angle of incidence with the beam different of zero using a double tilt cryo holder (at -170°C) in order to avoid sample irradiation damage and problems connected with the magnetic properties of iron material. For electron diffraction, an area of the order of 200 nm across was selected. On selected area electron diffraction patterns (SAED) were acquired with a camera length of 150 mm. Bright-field images and electron diffraction patterns were collected using a GATAN Orius 1000 CCD camera (11 Megapixel). Gatan Digital Micrograph software was used for evaluation of the data Background subtraction and radial integration of the 2D electron ring patterns were carried out using macros in the DiffTool package inside Digital Micrograph software [40].

X-ray absorption spectroscopy (XAS) can provide information on the atomic and molecular structure of materials, such as the oxidation state, ligand type and coordination geometry [41]. Scanning Transmission X-ray Microscopy (STXM), which uses the

Table 1
Peak positions on Raman spectra of carbonate phases.

Reference	Bernard et al. [30]	Savoie et al. [31]	Simpson and Melendres [32]	Saheb et al. [27]	Saheb et al. [33]
<i>Siderite</i> FeCO_3 Raman shift (cm^{-1})	282	275	290		
	495				
	733		520		
	1084 ^a	1082 ^a	734		
	1440		1080 ^a		
<i>Chukanovite</i> $\text{Fe}_2(\text{OH})_2\text{CO}_3$ Raman shift (cm^{-1})				131	
				200	238
					389
				382	
				498	
					534
					672
				730	730
				926	
			1071 ^a	1070 ^a	
				1434	
			1510	1510	

^a Main peak.

Table 2
Peak positions on Raman spectra of oxides phases.

Reference	Oh et al. [34]	Boucherit et al. [35]	De Faria et al. [36]	Thierry et al. [37]	Bersani et al. [38]	Demoulin et al. [39]
<i>Magnetite</i> , Fe_3O_4 Raman shift (cm^{-1})			302		311	
	532		513			
			534	550	541	
	667 ^a		663 ^a	670 ^a	666 ^a	
<i>Maghemite</i> , $\gamma\text{-Fe}_2\text{O}_3$ Raman shift (cm^{-1})		350	350	263		
	381			350		
	486			380		
		505	500	505		
	670	660		650		
	718 ^a	710 ^a	700 ^a	740 ^a		
	1425					
<i>Wüstite</i> , FeO						471
			652 ^a			653

^a Main peak.

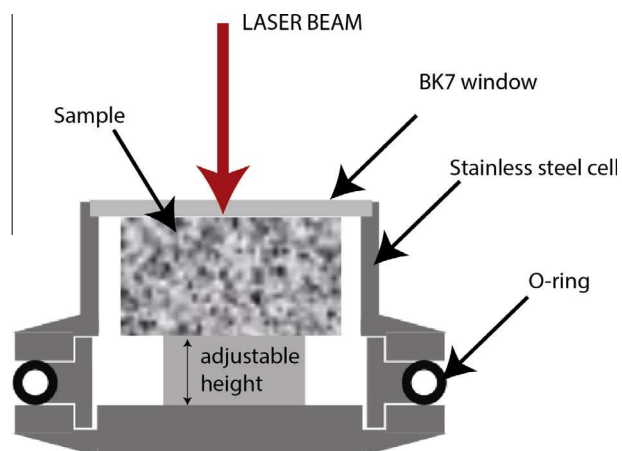


Fig. 1. Schematic of the Raman anoxic cell.

near-edge X-ray absorption fine structure (NEXAFS) can map the speciation of metals (e.g., oxidation state) with a very good spatial resolution [42]. STXM experiments were performed at the 10ID-1 beamline of the Canadian Light Source (CLS, Saskatoon) [43]. NEXAFS image sequences (i.e., stacks) were collected on the thin films at the Fe L- and C K-edges. The energy range and resolution of the scans were selected to obtain a good compromise between the total acquisition time (each image is collected in about 0.5–1 min, and an image sequence of 60–100 images in 1–2 h) and the needed resolution in the spectra parts containing information (i.e., L_2 and L_3 lines for Fe [15] and resonance peak at C K edge [44] – see Table 3). The measured transmitted signals (I) were converted to absorbance, also called optical density (OD), ($\text{OD} = -\ln(I/I_0)$) using the incident flux (I_0) measured in the absence of the sample. A set of reference spectra were collected of compounds (metallic iron, magnetite (Fe_3O_4), maghemite ($\gamma\text{-Fe}_2\text{O}_3$), siderite (FeCO_3) and chukanovite ($\text{Fe}_2(\text{OH})_2\text{CO}_3$)) suspected to be present in the samples, all of which were previously published [15].

Table 3
STXM scanning energy ranges and resolutions.

Edge	Region	Pre-edge	L ₃ region	Intermediary region	L ₂ region	Post-edge
Fe L	Energy range (eV)	698–704	704–713	713–719	719–725	726–780
	Resolution (eV)	0.6	0.15	0.4	0.15	3
Edge	Zone	Pre-edge	Resonance	Intermediary region	Post-edge	
C K	Energy range (eV)	280–283	283–295	295–310	310–320	
	Resolution (eV)	0.5	0.15	0.5	1.2	

Following the procedure described in detail elsewhere [15,42], the reference spectra were made quantitative by normalizing their intensity scales to an absolute linear absorbance scale (i.e., optical density per unit path length of a pure material of defined density) using the computed elemental response outside the structured near edge region [45], and the density of the material. To derive quantitative maps from the Fe L-edge image sequences Singular Value Decomposition (SVD) was used, which involved fitting the spectrum at each pixel to a linear combination of the quantitative reference spectra. The component maps are then expressed in equivalent thickness (nm). Suspected to be present [42]. The precision (statistical fluctuation) of the SVD fitting procedure is of the order of a few percent, and the accuracy in the absolute thicknesses of each component are mostly associated with systematic errors, on account that the elemental composition and/or density of the Fe species in the sample are different from that of reference spectral used in the fitting. However the relative magnitude and trends are expected to be independent of the systematic errors. To determine whether there was overlap of various Fe species signals in a component map (i.e., more than 1 component) curve fitting using a multiple linear regression procedure was used. The final fit selected was the one with the best χ^2 value without negative contribution from any reference spectra and the *F*-test value. All processing was performed using aXis2000 [46].

Before any cutting or preparation of transverse sections, sample GL10-03 was stored in a D₂O solution simulating the pore water of the Glinet soil (i.e., anoxic and carbonated with a HCO₃⁻ concentration of 7.8×10^{-3} M, for more details see [47]) for 3 months. After this treatment, and before thin film realisation, the metal–corrosion layer interface was investigated on a transverse section using NanoSIMS in order to study the penetration of the deuterated water into the corrosion layer.

Imaging H isotopic distributions and elemental ¹⁶O₂ and ⁵⁶Fe were performed on the Cameca NanoSIMS 50 of the National Ion MicroProbe Facility installed at the MNHN (Muséum Nationale d'Histoire Naturelle) in Paris. This instrument combines high sensitivity, high mass resolution and high spatial resolution allowing isotopic images to be obtained at the submicron scale. We acquired images covering areas of $50 \times 50 \mu\text{m}^2$ (512×512 pixels) and $15 \times 15 \mu\text{m}^2$ (256×256 pixels), on the transverse sections. A primary Cs⁺ beam was rastered over the sample surface with currents of 0.7 pA for elemental maps and 2.5 pA for H isotopes. Counting times were set to 1–4 ms pixel⁻¹. From 20 to 40 frames were collected to obtain one image with improved counting statistics. Prior to each analysis, the sample area was presputtered with a 50 pA Cs⁺ current for about 5 min to remove surface contamination and the gold coating and to implant Cs⁺ into the sample. Secondary ion images of ¹H and ²D were simultaneously recorded. Since it was not possible to acquire simultaneously H–D with heavier isotopes the ¹⁶O₂, and ⁵⁶Fe were done in separate experiments at the same locations where H isotopes were measured. Images and data were processed using the LIMAGE software (developed by L. Nittler, Carnegie Institution, Washington DC, USA) and corrected for detector dead time (44 ns) and secondary ion images drift in X and Y positions. It was then possible to calculate isotopic D/H ratios and to extract profile distribution of this ratio and on local ¹⁶O quantity.

4. Results

Results from former studies on archaeological nails from Glinet [28] are confirmed by micrometre scale observations made on transverse sections: the total thickness of the corrosion products is about several 100 μm , mainly consisting of ferrous carbonates (siderite) or hydroxycarbonates (chukanovite). In some case, microscopic islets of magnetite were found in the carbonates. The detailed description of the corrosion patterns will not be questioned here and can be found elsewhere [48]. Let us now focus on the metal–corrosion product interface.

SEM–FEG Back Scattered Electron (BSE) images (Fig. 2) on the transverse sections of the four archaeological nails show that the corrosion products are composed of different layers evidenced by the chemical contrast. On all samples, there is a continuous layer between the metallic core and outer corrosion products, hereafter referred to as the interfacial layer. This interfacial layers appears lighter than the outer corrosion products suggesting a higher atomic mass. Generally the interfacial layer thickness is lower than 500 nm and is hardly observable (Figs. 2c and 1d), however, in a few places this layer reaches several μm (Figs. 2a and 1b). These low thicknesses explain why Saheb et al [48] did not found an interfacial layer using a classical SEM (with a lower spatial resolution). It should also be noted that lighter zones appear throughout the outer layer, particularly near the interfacial layer, suggesting some phase mix in the outer layer. EDS maps suggest that the interfacial zone is richer in Fe than the outer layer (Fig. 3).

Fig. 4 shows representative μRaman spectra (siderite, chukanovite, magnetite and a magnetite/maghemite) obtained from the nails interfacial and outer layers and the Raman maps of the thick region of interfacial layer of two nails, derived by the ROI method, showing the distribution of magnetite, siderite and chukanovite. The results verify that the outer layer is made of carbonates, mainly as siderite, while the interfacial layer consisted of iron oxides, mainly as magnetite. On some samples small areas of chukanovite were also observed (Fig. 3a). It can be stressed that no carbonated green rust was found in the carbonated zones of the outer layer. Note also that on some samples, the interfacial layer seems to be made of a mix of magnetite and maghemite ($\gamma\text{-Fe}_2\text{O}_3$) as evident from an extracted spectra (Fig. 4c). A summary of the μRaman results can be found in Table 5.

TEM observations were performed on sample GL10-03, on the thinner interfacial layer (<500 nm) (Fig. 5a). Electron Diffraction (ED) patterns from the interfacial layer (zone 2), after circular integration were compatible with both magnetite and/or maghemite (not distinguishable by ED), while those obtained from the outer layer (zone 1) of the corrosion products are in good agreement with that of siderite (Fig. 5b and c). These observations at higher magnification also suggest that the interfacial layer, despite presenting very variable thickness, seems continuous around the metal.

STXM analysis at the Fe L-edge was performed on thin films taken at different places along the metal/corrosion products interface for the different nails (GL10-03, GL10-01, GL07-40). Similar results were obtained for all the nails, and they were similar to the GL10-04 nail previously reported on [15]. Fig. 6 is a typical

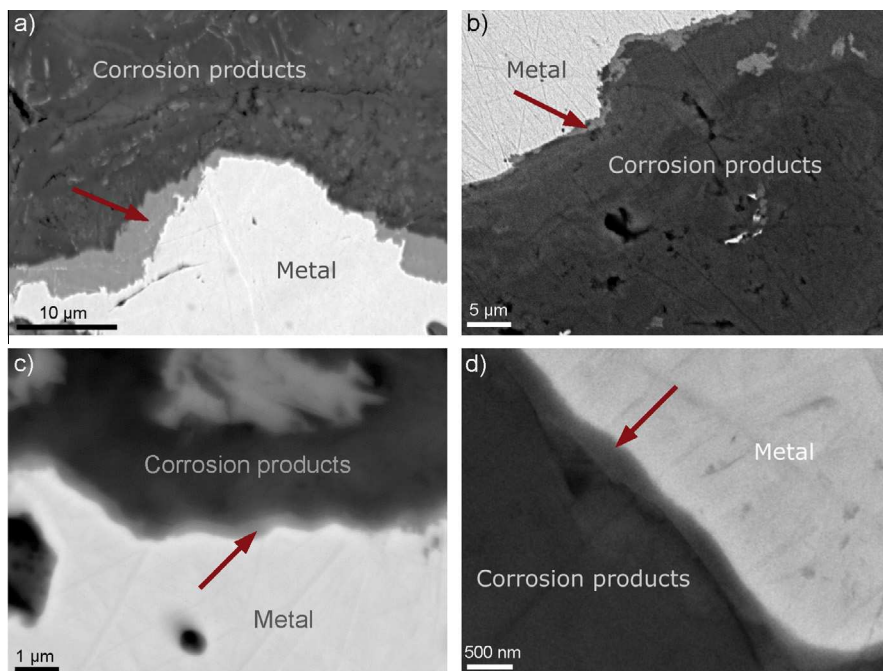


Fig. 2. SEM–FEG Back Scattered Electron microphotographs of the transverse sections of the archaeological nails, arrows indicate the location of the interfacial layer (a) GL10-03, (b) GL10-04, (c) GL10-01 and (d) GL-10-03. The thickness of the interfacial layer varies from several hundred nanometres (c and d) to several micrometres (a and b).

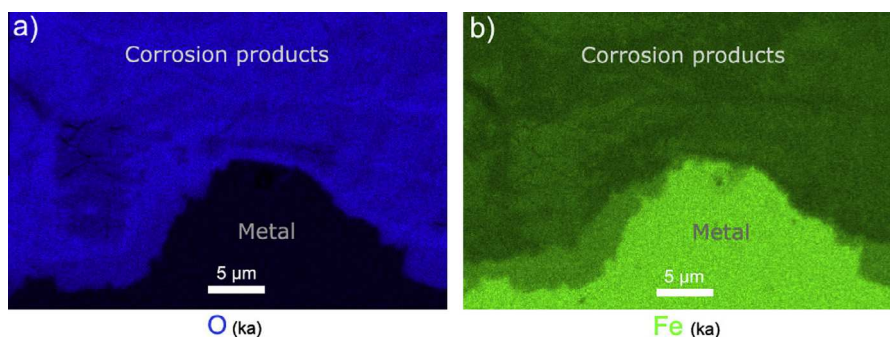


Fig. 3. EDS maps at the metal – corrosion product interface of the sample cross-section GL10-03: (a) O ($K\alpha$), and (b) Fe ($K\alpha$).

example and shows the Fe(0), Fe(II) and Fe(III) component maps derived from the SVD spectral fitting of the image sequences from the GL10-03 nail, using the reference spectra of metallic iron (Fe(0)), siderite (Fe(II)) and maghemite (Fe(III)). The choice of the Fe(II) and Fe(III) reference spectra for the SVD analysis was selected because their Fe 2p line shapes were characteristic for that of most Fe(II) and Fe(III) species and they were similar to spectra manually extracted from the image sequences (see Fig. 8). Note that the spatial distribution of the Fe(II) and Fe(III) components in the nail would have been similar using other Fe(II) and Fe(III) reference spectra with similar Fe 2p line shape [15]. The difference in the component maps using different reference spectra for the fitting would be in the absolute equivalent thicknesses (nm) determined (i.e., y-scale) but the trends would be expected to be similar. The interfacial layer consisted predominantly of Fe(III) species, while the outer layer consisted predominately of Fe(II) species. As observed by SEM and TEM, depending on its location on the sample, the layer can be relatively thick (about 1 μm on GL10-03, Fig. 6) but also sometimes much thinner (about 100 nm GL10-01, Fig. 9a). Fig. 6c shows the image difference map (290–280 eV) of the thin film. This allows to reveal the location of carbonates because of the typical peak classically observed on carbonate

spectra acquired at C K-edge around 290 eV (see Fig. 7). The boundary between the interfacial layer and outer layer is evident, and carbonate concentration is considerably higher in the outer layer than that of the interfacial layer, which is consistent with the outer layer being composed of Fe(II) carbonates and the interfacial of Fe(II,III) containing phases. The presence of these latter phases with higher iron oxidation degree at metal/oxide interface was observed by several authors [18–22] and will be commented in the discussion.

To gain further insight into the chemical nature of the Fe in the interfacial and outer layers, spectra were extracted from these layers by averaging all the pixels corresponding to the interfacial layers and then these spectra were curve fit using the reference spectra of iron, siderite, chukanovite, magnetite and maghemite. Fig. 8 presents curve fitting results obtained on nail GL10-03. The best curve fit obtained of the spectrum from the outer layer, without negative contribution ($\chi^2 = 0.19$), is a combination of 41 nm of chukanovite, 10 nm of siderite and 6 nm of maghemite. This confirms that the main Fe species in the outer layer are carbonates. The presence of very low quantities of Fe(III) species in this layer will be commented below. The best curve fit obtained of the spectrum from the interfacial layer is a mix of magnetite (15 nm) and

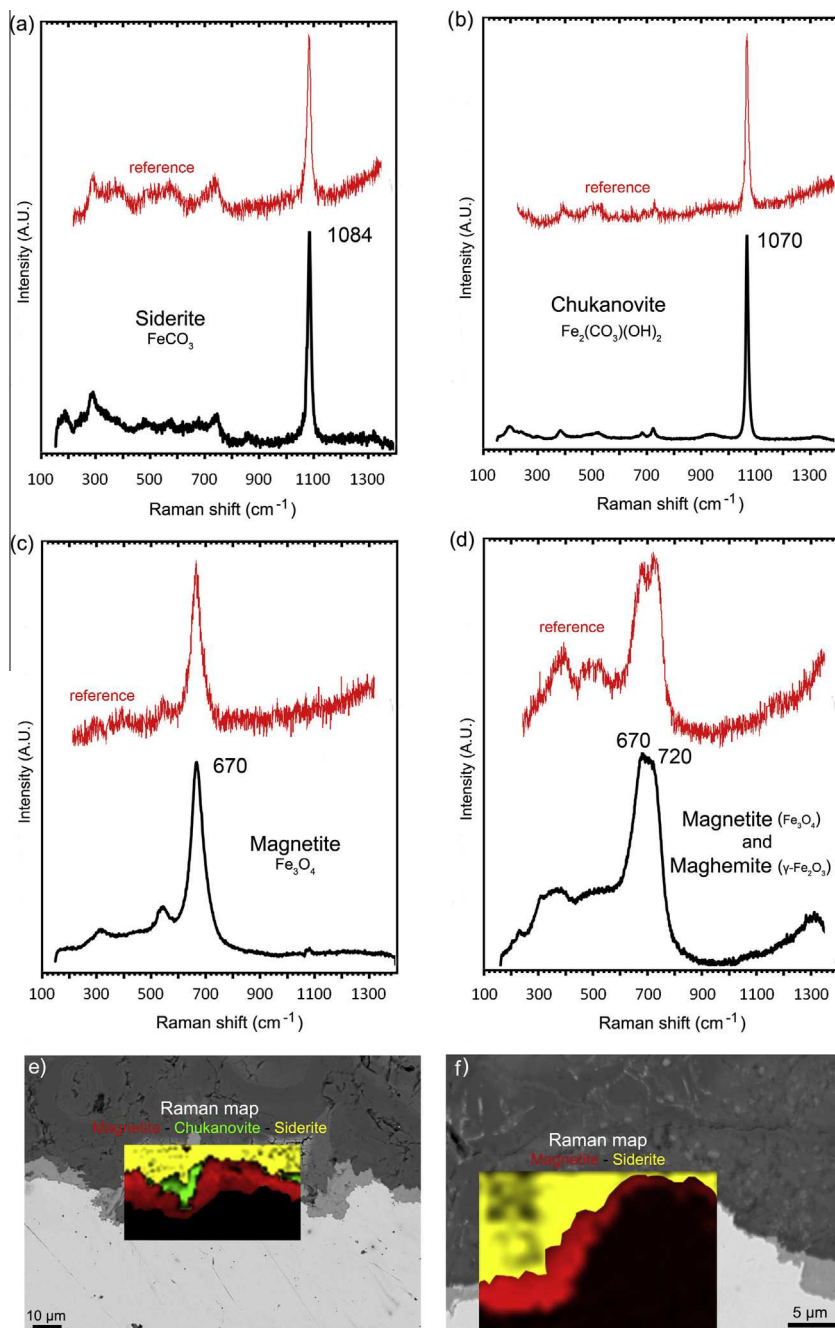


Fig. 4. Representative Raman spectra: (a) siderite on sample GL07-40, (b) chukanovite sample GL07-40, (c) magnetite at the interfacial layer of the sample GL07-40 and (d) magnetite–maghemite mix at the interfacial layer of the sample GL10-01. SEM–FEG BSE microphotographs with the corresponding Raman distribution maps of magnetite (red), siderite (yellow) and chukanovite (green), at the metal – corrosion product interface of the samples cross-sections: (e) GL07-40 and (f) GL10-03. Dotted square: zone where nanoSIMS analyses were performed. (For interpretation of the references to colour in this figure legend, the reader is referred to the web version of this article.)

maghemite (27 nm). The best curve fit ($\chi^2 = 0.77$) for the interfacial layer from the GL10-01 nail showed on Fig. 9, corresponded to a mix of maghemite (28 nm), magnetite (10 nm), carbonates (siderite and chukanovite: 27 nm) and iron (8 nm). The oxide phases are the majority and the presence of carbonates and metallic iron can be explained by the fact that the layer is thinner at this location than the STXM resolution. Table 4 summarizes the results of the curve fits obtained on spectra extracted from the interfacial zone of all analysed samples. If one does not consider the scarce presence of carbonates or metal due to the difficulty to extract signal coming only from the very thin interfacial layer (GL10-1 and GL07-40), one can observe that all interfacial layer spectra can be

modelled satisfactorily using a combination of maghemite and magnetite. It is interesting to note that the maghemite/magnetite ratio is between 1.8 and 3.5.

The observations performed by STXM are consistent with the ones obtained by other techniques and bring more information at the sub-micrometre level. The outer part of the corrosion layer consists mainly of carbonates with a trace amounts of Fe(III). The presence of Fe(III) species in the carbonate layer was previously observed by a former study [48]. But until now, they were more associated to larger microscopic zones of iron oxides (magnetite) in the layer. Besides, between carbonates and the metal, at nano-metre scale, an interfacial layer is evidenced constituted of a mix

Table 4

Phase proportion (equivalent thickness) deduced from the curve fits on NEXAFS spectra extracted from the interfacial layers.

Samples	Combination of reference phases	Equivalent thicknesses (nm)	Magnetite/maghemite ratio
GL10-03 A1	Maghemite/magnetite	39/12	3.25
	Maghemite/magnetite/iron	33/12/8	2.75
GL10-03 A2	Maghemite/magnetite	27/15	1.8
GL10-03 A3	Maghemite/magnetite	28/14	2
GL10-04 ^a	Maghemite/magnetite	30/13	2.31
GL10-01	Maghemite/magnetite/siderite/chukanovite/iron	28/8/13/14/8	3.5
GL07-40	Maghemite/magnetite/siderite/iron	18/10/25/61	1.8

^a Published in [15]. A1, A2 and A3 correspond to three different thin films taken on the same nail.

of iron oxides. The important part of Fe(III) phases at this location can be emphasised. Actually, in the interfacial layer, pure zones of magnetite were never observed by STXM contrary to the results given by μ Raman spectroscopy (with the latter techniques, pure magnetite zones were found at micrometre level on GL07-40 and GL10-03). This could be explained by different reasons. First, slight reoxidation of some zones during FIB sampling can be evoked. Nevertheless this effect seems to be very limited because of the fact that pure iron spectra are obtained on the metallic part (see [15]). The fact that pure magnetite zones were not found, could

also be explained because the thin film made for STXM was not taken exactly at the same place as the one of the μ Raman observation. Lastly, despite a slight re-oxidation effect cannot be totally excluded, the consistency of all the observations and the fact that even with μ Raman (during which anoxic conditions were drastically respected) mixed zones of maghemite and magnetite were also observed on two of the four examined samples, suggest that this interfacial layer of variable thicknesses (from several μ m to several 100 nm) is made of a mixture of iron oxides containing both Fe(II) and Fe(III) valences (magnetite and maghemite) with variable proportions. The present techniques do not allow to determine if this corresponds to a dual layer as suggested by some authors for the passive nanometric film formed in borate buffer on iron [20,49,50], or other metals [51].

The $^{16}\text{O}_2$ and D/H ratio distribution were examined using nano-SIMS (after the Raman measurements, Fig. 3b) in the transverse section of the GL10-03 nail immersed, before any other treatment, in D_2O for 3 months (Fig. 10). The $^{16}\text{O}_2$ distribution map clearly shows that the corrosion products can be differentiated from the metal. Note, there was a crack going through the corrosion products in the middle of the map as evident by the absence of oxygen and the depletion in the D/H ratio but it has no bearing on the interpretation of the results and will not be discussed further. Fig. 11 plots the profile extracted from the $^{16}\text{O}_2$ and D/H ratio distribution maps (Fig. 10). The two profiles were normalised to show the same value at their plateau in the corrosion products. The interface between the metal and corrosion products was apparent from an abrupt change in the $^{16}\text{O}_2$, gradually increasing and

Table 5

Summary of the characterisation results obtained on the different samples.

Sample	Outer layer	Interfacial layer			
		Thickness	μ Raman	STXM	TEM
GL10-01	S, C	<500 nm	Mag/Mah mix	Mah/Mag/S/C Iron	Iron oxide
GL10-03	S, C	<100 nm to several μ m	Mag/Mah layers pure mag layers	Mag/Mah mix	Iron oxides
GL10-04 ^a	S, C	< μ m to several μ m	Mag/Mah mix	Mag/Mah mix	
GL07-40	S, C	<100 nm to several μ m	Mag/Mah layers pure mag layers	Mag/Mah mix	

S: siderite, C: chukanovite, Mah: maghemite, Mag: magnetite.

^a From [15].

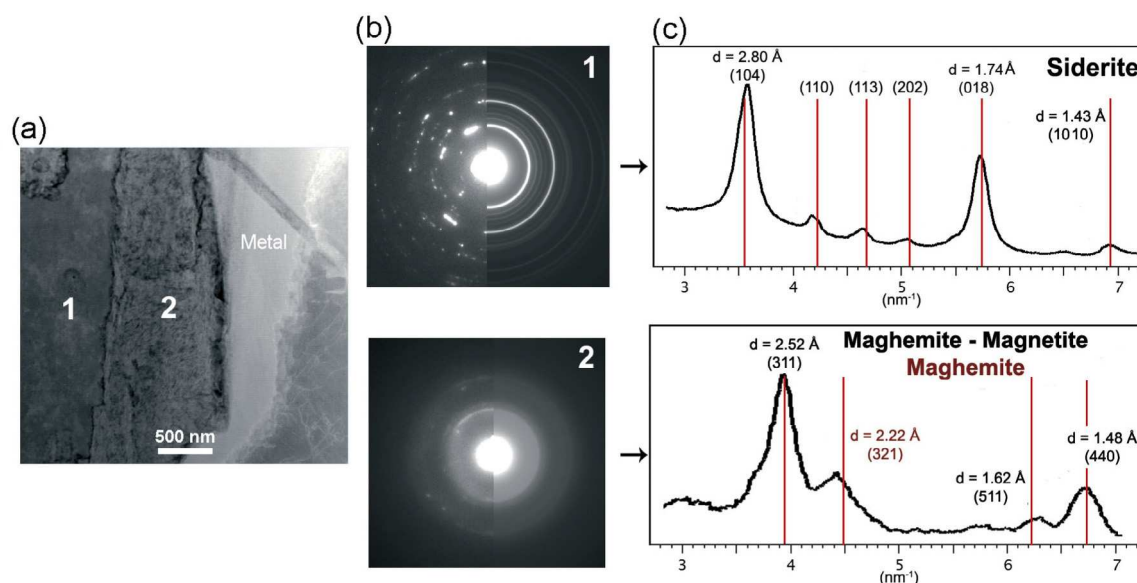


Fig. 5. TEM microphotographs of the sample thin film GL10-03: (a) bright-field images of the metal, interfacial layer (zone 2) and outer layer (zone 1), (b) diffraction patterns of the siderite (top) obtained in zone 1 and mix of magnetite–maghemite (bottom) from the interfacial layer (zone 2), and (c) radially integrated diffraction data.

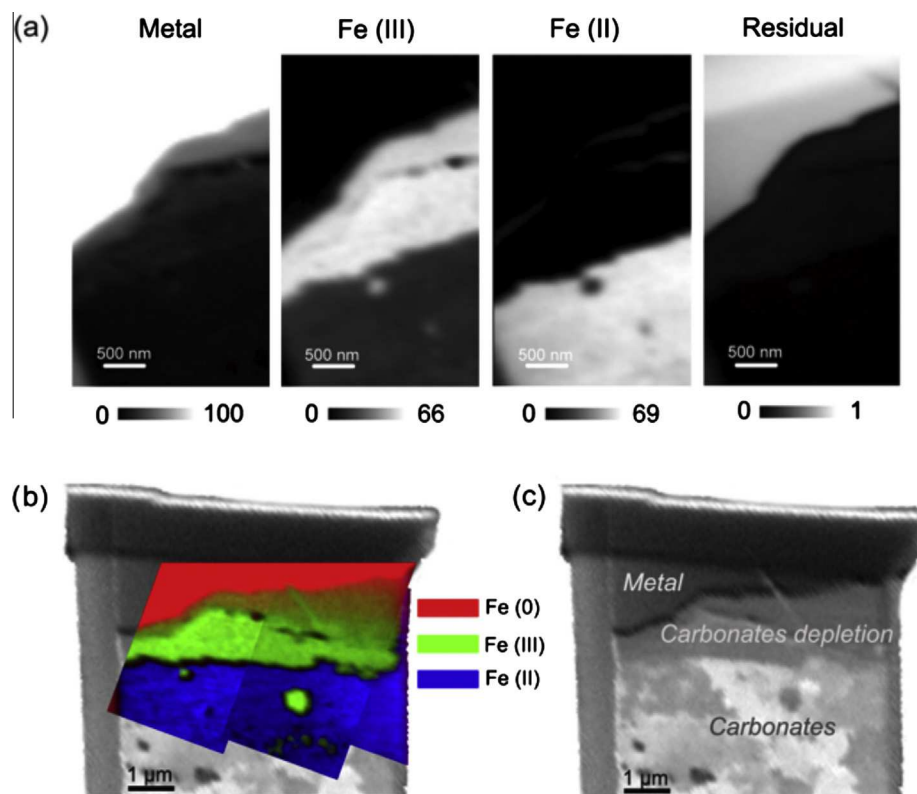


Fig. 6. STXM investigations of the sample thin film GL10-03: (a) SDV component maps of the Fe(III), Fe(II) and Fe(0) species obtained with the siderite, maghemite and metal reference spectra. Grey scales for Fe(II), Fe(III) and Fe(0) maps: equivalent thickness (nm), for the residual map: optical density. (b) Overlay of the color-coded Fe(0), Fe(II) and Fe(III) component maps (c) C K-edge difference map (290–280 eV) of the thin film.

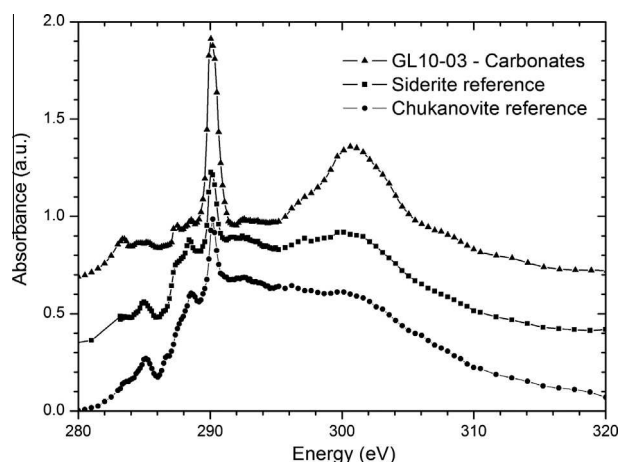


Fig. 7. STXM spectrum extracted from the carbonate zone compared to the one obtained on siderite and chukanovite references (C K edge).

thereafter levelling off. It is interesting to note that the D/H ratio abruptly changed about 1.5–2 μm further away from the metal/corrosion interface. This distance is on the same order of magnitude as the thickness of the interfacial zone at this location (see Figs. 3 and 4).

The increase in the D/H ratio is obviously due to the penetration of D_2O into the pore network of the corrosion products during the re-corrosion treatment. This high D content can be linked to hydroxyl deuterated groups in the chukanovite or to adsorbed deuterated water in the surface of the pores (a small quantity of D_2

could have been produced by iron corrosion but can be considered as negligible compared to the two other cases) [33,47]. At this location, as shown on Fig. 4b only siderite and iron oxides were detected by μRaman investigations, but no chukanovite. This suggests that the increase of the D/H ratio is not due to chukanovite containing D, but to adsorbed water in the pore network. Because no phase containing H (or D) were detected in the outer corrosion products nor in the interfacial layer, the fact that a D/H decrease is observed in the interfacial layer strongly suggests that this layer is much less porous than the rest of the corrosion products. The depleted zone is slightly thinner than the oxide one, suggesting that the inner part of the interfacial layer, in contact with the metal is nonporous but the outer one a little more. This must be investigated deeper in future work at nanoscale. In any event, this important observation corroborates the potential protective role of the interfacial layer in the corrosion process, and its influence on the kinetics evocate by some authors [52].

5. Discussion

Table 5 sums up the results obtained from the different methods used to examine the nails. These different methods were employed here to better understand the system and particularly the nature of the interfacial layer. We must keep in mind that they implement different kind of radiations and particles (photons, electrons, ions) implying different penetration depths and consequently different investigated volumes. Nevertheless, the great consistency of the results obtained by these different approaches and analytical methods seems to strengthen the general observations made on the complete set of samples. All the nails examined

had a continuous interfacial layer between the metal and outer carbonated corrosion products. The interfacial layer thickness was more often of several 100 nm but in some places it reached 1 μm . At the nanoscale it was composed of a mix of iron oxides with various Fe(II)/Fe(III) proportions. Pure Fe(III) phase (maghemite) was never identified despite Fe(III) seems to be the predominant iron valence. Besides, the presence of low quantities of Fe(III) containing species in the Fe(II) carbonated layer identified by STXM suggest a competition between the interfacial layer and the carbonate layer.

The same kind of interfacial layer was found by several authors on mild steel corroded in aqueous environments saturated with CO_2 [19]. In the present study also, an interfacial layer of iron oxides was found between the metallic substrate and a thick outer layer of Fe carbonates (siderite and chukanovite but no carbonated green rust). Actually, the same kind of mechanism proposed by these authors can be used to explain magnetite formation on

archaeological artefacts corroded in anoxic carbonated media. First, let us recall that in some cases a mill scale made of a mix of magnetite, hematite and wustite can sometimes initially embed the iron archaeological artefacts [39,48,53,54]. This outer mill scale must not be confused with the interfacial scale considered here. It is not protective and does not hinder the formation of siderite. The latter phase is indeed, the one that is thermodynamically stable in the beginning of the corrosion process in the water of the archaeological site of Glinet [48]. On the contrary, the mill scale tends to disappear during the long term corrosion process. After several centuries of corrosion, traces of the initial mill scale can be found on some artefact in the external part of the corrosion layers but will no more be considered in the following.

Considering these results on the physico-chemical characterisation of the system, some hypotheses on possible mechanisms can be discussed based on mechanisms already proposed in literature and basic thermodynamic considerations. This must be completed

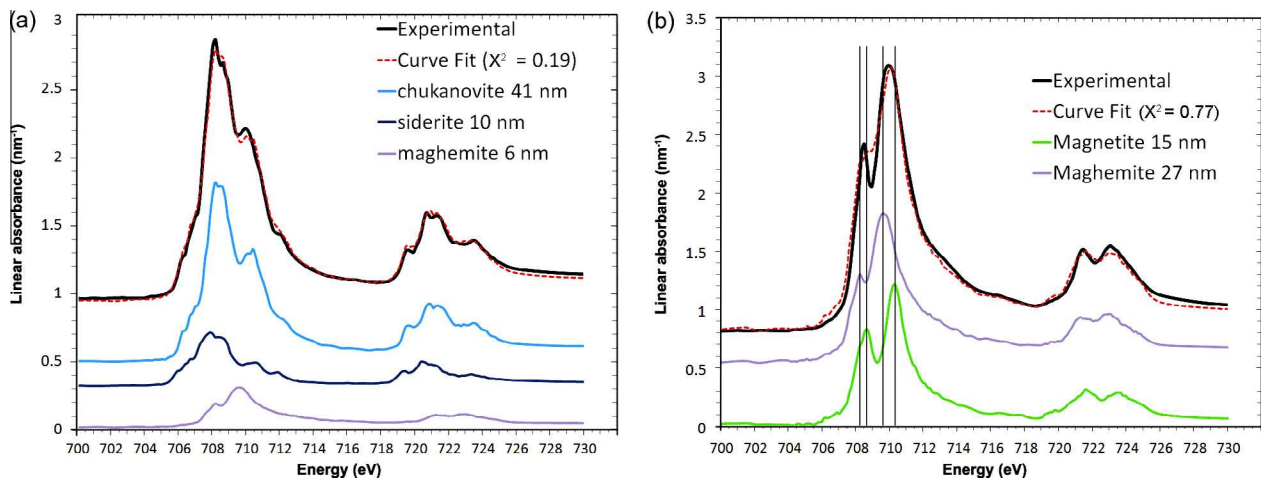


Fig. 8. Curve fits of the averaged spectrum extracted from the (a) outer and (b) interfacial layers of the GL10-03 thin film. Reference spectra: chukanovite, siderite, magnetite and/or maghemite. Deduced equivalent thicknesses (nm).

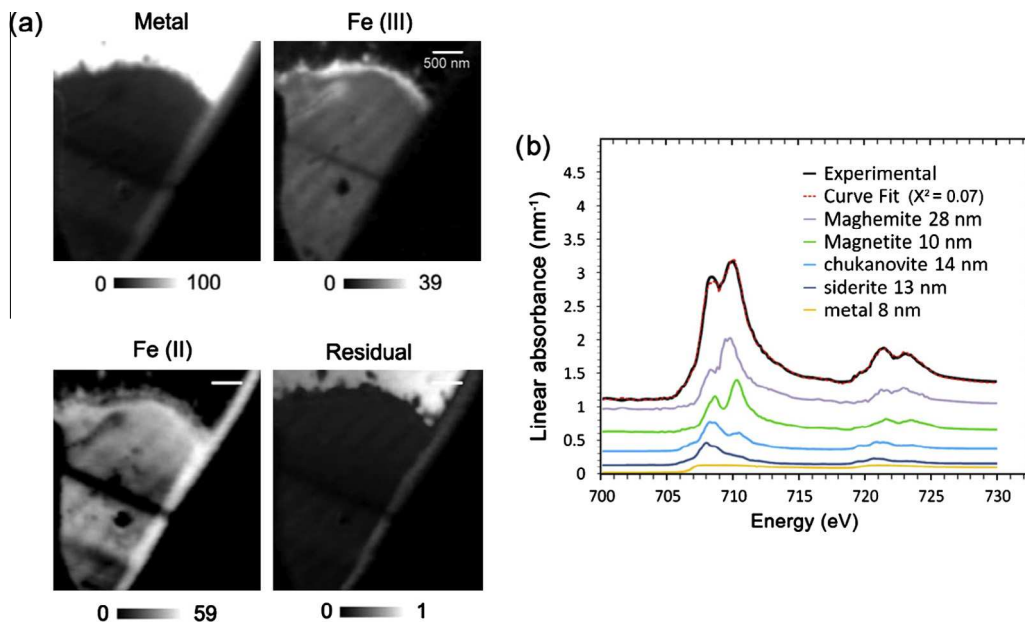


Fig. 9. STXM investigations of the sample thin film GL10-01: (a) SDV component map of the Fe(III) species using siderite, maghemite and metal reference spectra. (b) Spectrum extracted from the Fe(III) zone of the thin film (white area), reference spectra and linear fit.

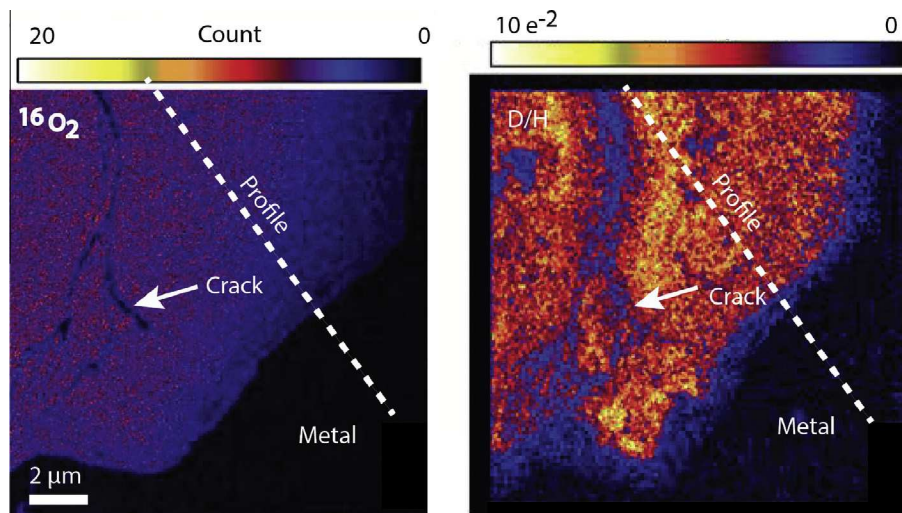


Fig. 10. nanoSIMS maps of $^{16}\text{O}_2$ and D/H ratio obtained at the Metal/Corrosion products interface on sample GL10-03.

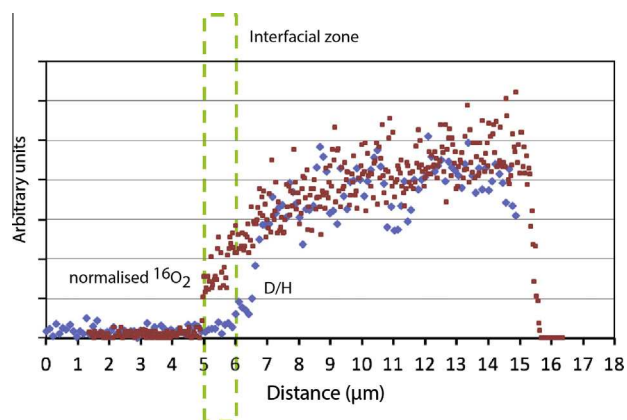
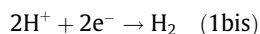
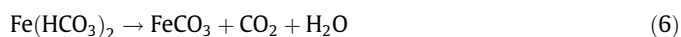


Fig. 11. $^{16}\text{O}_2$ and D/H profiles extracted at the location indicated on Fig. 10. $^{16}\text{O}_2$ profile maximum was normalised to correspond to the one of D/H.

in the future by considerations on reactivity of the phases and kinetics. If one considers the corrosion process without this mill scale, the initial water composition and especially the neutral pH leads to the following possible cathodic reactions



Consequently siderite can precipitate on the nail following different paths [22]:



Despite Pourbaix diagrams give only a thermodynamic approach that does not account for the kinetics of the phase formation, it is a very useful first stage to understand the system. The

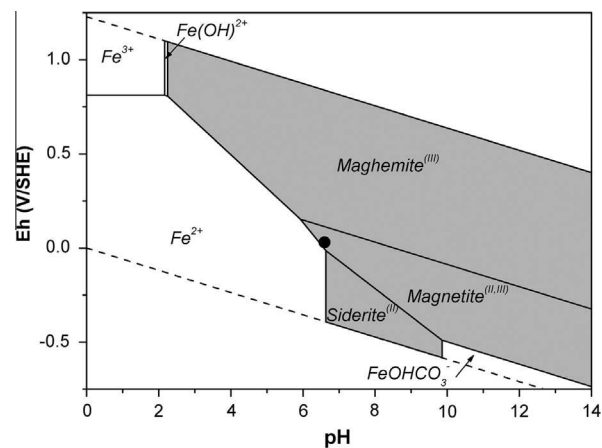


Fig. 12. Eh vs pH Pourbaix diagram. Composition of water for calculation: see Table 6. Black circle: Glinet water composition. The precipitated phases are in grey and the aqueous ones are in white. Thermodynamic data from [55,56].

diagrams presented on Figs. 12–14 have been drawn based on thermodynamic data from literature (see Table 7). Calculations were made using a simplified water composition close to the one of Glinet (Table 6). The Pourbaix diagram (Fig. 12) has been calculated taking into account a simplified composition representative of the Glinet water (Table 6 and [47]). The black circle indicates the conditions measured on the Glinet site where the nails were taken. It indicates that the Glinet water composition does not allow the direct appearance of chukanovite ($\text{Fe}_2(\text{OH})_2\text{CO}_3$). Nevertheless, a decrease of the carbonate content (as suggested by the diagram on Fig. 13 presenting the correlation between carbonate and iron concentration for the pH of the Glinet site) and/or a pH increase could favour chukanovite appearance. Some other authors suggest that a third phase could form at lower carbonate concentration: the carbonated green rust ($\text{GR}(\text{CO}_3^{2-})$ or $(4\text{Fe}(\text{OH})_2 \cdot 2\text{Fe}(\text{OH})_3\text{CO}_3)$) [23,24]. The fact that this latter phase was not observed in the present study could be explained by its low thermodynamic stability. These authors argue that it could transform in magnetite. This could be an explanation for the presence of low quantity of Fe(III) species in the carbonate outer layer observed by STXM.

Because of the precipitation of the phases, the layer of corrosion products (mainly formed of siderite), become more and more compact with time as suggested by former studies on the Glinet nails

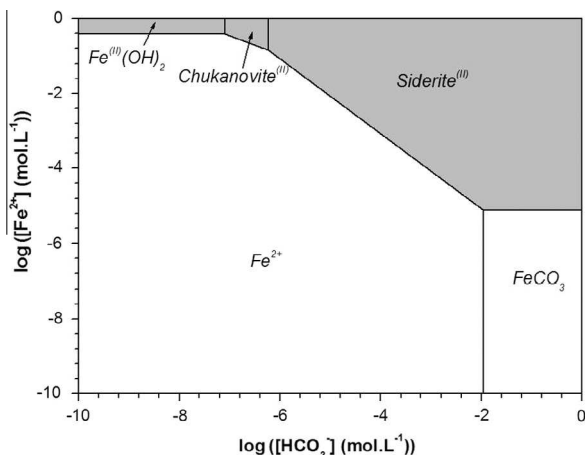


Fig. 13. Correlation between carbonate and iron concentration for the pH of the Glinet site (pH = 6.5). Composition of water for calculation: see Table 6. Thermodynamic data from [55,56].

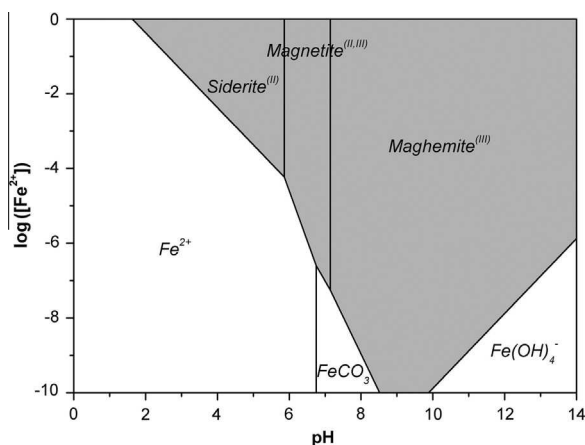
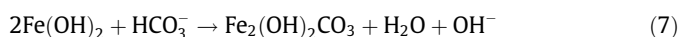


Fig. 14. Log(Fe) versus pH diagram at Eh = 0.1 V/SHE. Composition of water for calculation: see Table 6, Thermodynamic data from [55,56].

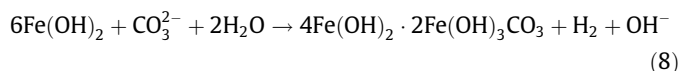
[47,57]. This decrease of carbonate porosity retards the replenishment of protons, which are consumed by iron corrosion processes at the metallic interface, leading to the pH increase at this interface. This pH increase could also be accelerated by the production of OH⁻ following Eq. (1). Lastly it can be supposed that the pH increase is slowed in case of chukanovite formation because of the consumption of OH⁻ ions. Nevertheless, some authors [58] also report the transformation of Fe(OH)₂ metastable species into chukanovite, releasing a OH⁻ ions that could have an increasing effect on the pH:



Fe(OH)₂ was not identified here but it has to be stressed that this metastable phase was only detected in in-situ studies, for example by [59]. The same for the possible green rust formation mentioned by [23,24]:

Table 7
Thermodynamic data used for modelling the environmental conditions.

Equation	Thermo. constant	Reference
$\text{Fe} + 2\text{H}^+ + 1/2\text{O}_2 \rightarrow \text{Fe}^{2+} + 2\text{H}_2\text{O}$	$\text{p}K_a = 57.5019$	[55]
$\text{Fe}^{3+} + 1/2\text{H}_2\text{O} \rightarrow \text{Fe}^{2+} + \text{H}^+ + 1/4\text{O}_2$	$\text{p}K_a = -7.7776$	[55]
$\text{FeCO}_3 + \text{H}^+ \rightarrow \text{Fe}^{2+} + \text{HCO}_3^-$	$\text{p}K = 4.6452$	[55]
$\text{Fe}(\text{OH})_4^- + 4\text{H}^+ \rightarrow \text{Fe}^{3+} + 4\text{H}_2\text{O}$	$\text{p}K = 21.6383$	[55]
$\text{FeOH}^{2+} + \text{H}^+ \rightarrow \text{Fe}^{3+} + \text{H}_2\text{O}$	$\text{p}K = 2.1638$	[55]
$\text{FeOHCO}_3^- + 2\text{H}^+ \rightarrow \text{Fe}^{2+} + \text{H}_2\text{O} + \text{HCO}_3^-$	$\text{p}K = 14.3829$	[55]
Ferrous hydroxide $\text{Fe}(\text{OH})_2 + 2\text{H}^+ \rightarrow \text{Fe}^{2+} + 2\text{H}_2\text{O}$	$\text{p}K_s = 12.7843$	[55]
Magnetite $\text{Fe}_3\text{O}_4 + 8\text{H}^+ \rightarrow \text{Fe}^{2+} + 2\text{Fe}^{3+} + 4\text{H}_2\text{O}$	$\text{p}K_s = 10.1642$	[55]
Maghemite $\text{Fe}_2\text{O}_3 + 6\text{H}^+ \rightarrow 2\text{Fe}^{3+} + 3\text{H}_2\text{O}$	$\text{p}K_s = 3.3076$	[55]
Siderite $\text{FeCO}_3 + \text{H}^+ \rightarrow \text{Fe}^{2+} + \text{HCO}_3^-$	$\text{p}K_s = -0.4731$	[55]
Chukanovite $\text{Fe}_2(\text{OH})_2\text{CO}_3 + 3\text{H}^+ \rightarrow \text{Fe}^{2+} + 2\text{H}_2\text{O} + \text{HCO}_3^-$	$\text{p}K_s = 11.8829$	[56]



A consequence of this pH increase is a change of the local conditions going out of the predominance domain of carbonates (Fig. 12) to reach the one of magnetite, conducting to the precipitation of this phase at the metal oxide interface. It can be assumed that the thickness of the oxide layer is linked to the local access of protons at the external zone of the interfacial layer, directly correlated to the local porosity of the carbonate layer.

Indeed, in the case of the Glinet samples, the layer is not constituted by pure magnetite but by a mixture of oxides or by a phase containing more Fe(III) species than magnetite. This fact was also observed in studies on mild steel corroded in anaerobic borate buffer solutions by Davenport et al [49], performing grazing incidence X ray diffraction. The best fit of the diffraction pattern they obtained suggests a nanocrystalline phase with a stoichiometry of Fe_(1.9+2)O₃ in which most of the Fe cations are in Fe³⁺ state [60]. The presence of relatively important proportion of Fe(III) species could be explained, by some local pH variation. As suggested in Fig. 14, for a given Eh of +0.1 V, a slight increase in pH could favour the formation of maghemite.

The particularity of the archaeological artefacts compared to laboratory or short-term corroded samples, is that the thickness of the interfacial layer varies very locally from several 100 nm to several μm. Actually this variation of thickness could be explained by local differences of porosity of the embedding carbonate layer, controlling the access of H⁺ ions and consequently the pH. One can suppose that, if the pH is sufficiently basic, the oxide layer can grow but, as soon as the outer layer is sufficiently cracking and getting less dense, it allows the penetration of H⁺ ions causing a pH drop, so that the oxide layer is no more stable and dissolves at its outer interface. This heterogeneous and progressive dissolution could also explain the trace of Fe(III) species in the carbonate. The outer border of the interfacial zone would then delimitate a iso-pH line.

Besides, even when the interfacial layer is relatively thick, NanoSIMS D labelling experiments strongly suggest that this layer is much less porous than the outer corrosion products made of carbonates. Consequently it can hinder the water penetration and contact with the metallic substrate. Indeed, probably only the inner part of the interfacial layer presents a low porosity, that increases in the outer part of the thick interfacial layers. Neverthe-

Table 6
Composition of the solution used for thermodynamic modelling.

Species	[Fe ²⁺]	[HCO ₃ ⁻]	[Ca ²⁺]	[Cl ⁻]	pH	Eh
Concentrations (M)	1×10^{-5}	7.8×10^{-3}	3.5×10^{-3}	3.5×10^{-4}	6.5	0.1/SHE
Dissolved salts	(NH ₄) ₂ Fe(SO ₄) ₂ , 6H ₂ O	NaHCO ₃	CaSO ₄	NaCl		

less the fact that at least a part of the interfacial layer is much less porous confirms the hypothesis that the interfacial layer potentially controls the kinetics. It is now of primary interest to study more precisely the mechanisms involved and consequently the physico-chemical properties of this layer (conductivity and porosity) in order to confirm or not if models as the one proposed by Bataillon et al. [52] and based on the control of the kinetics by solid state transport (ions and vacancies) in the layer is valid here.

6. Conclusions

This study on four archaeological nails corroded in an anoxic carbonated environment confirms the presence of an iron oxide (Fe(II), Fe(III)) interfacial layer between the metal (Fe(0)) and the outer carbonated corrosion (Fe(II)) layer. The thickness of the interfacial layer varied between 100 nm to several μm . The iron oxide in the interfacial area was composed of a mixture of magnetite and maghemite. The layer could form after a pH increase at the interface provoked by the consumption of H^+ ions during the corrosion processes. D_2O labelling experiment coupled to nanoSIMS mapping of the D/H ratio at the interface strongly suggest that this layer is significantly less porous than the outer carbonated corrosion products. This could imply that the corrosion kinetics in carbonated anoxic media are controlled by this layer. Further experiments must be conducted on this layer to precise the way this kinetics are controlled and the parameters that influence its thickness. Moreover the next crucial perspective will be to consider the local reactivity and conductivity of the different parts of these complex layers using adapted micro electrochemical methods.

Lastly, if the controlling role of the interfacial layer is confirmed, it will be necessary, in further studies, performed on samples coming both from laboratory experiments and other archaeological sites on which the same environmental conditions were observed (e.g., Nydam Mose in Denmark [61]) to confirm these first crucial results on a wider set of samples.

Acknowledgements

The team of Cameca NanoSIMS 50 installed at the MNHN (Muséum Nationale d'Histoire Naturelle) and especially Smail Mostefaoui and Remi Duhamel, Jean-Paul Gallien for the D_2O setup and anoxic cell design, Enrique Vega for the SEM-FEG measurements are gratefully thanked. This work was partly founded by the Groupement de Laboratoires "Verre-Fer-Argile" of ANDRA.

References

- [1] F.F. Eliyan, A. Alfantazi, Mechanisms of Corrosion and Electrochemical Significance of Metallurgy and Environment with Corrosion of Iron and Steel in Bicarbonate and Carbonate Solutions – A Review, *Corros. Sci.* <http://dx.doi.org/10.5006/1213> (in press).
- [2] E. Shelton, A.B. Rothwell, R.I. Coot, Steel requirements for current and future Canadian gas pipeline systems, *Met. Technol.* 10 (1983) 234–241.
- [3] F. Farelais, M. Galicia, B. Brown, S. Nestic, H. Castaneda, Evolution of dissolution processes at the interface of carbon steel corroding in a CO_2 environment studied by EIS, *Corros. Sci.* 52 (2010) 509–517.
- [4] A. Clanfield, F. Cattant, D. Crusset, D. Feron, Corrosion issues in nuclear industry today, *Mater. Today* 11 (2008) 32–37.
- [5] D. Feron, D. Crusset, J.M. Gras, Corrosion issues in the French high-level nuclear waste program (reprinted from proceedings of the CORROSION/2008 research topical symposium), *Corrosion* 65 (2009) 213–223.
- [6] D.A. Scott, G. Eggert, Iron and Steel in Art: Corrosion, Colorants, Conservation, Archetype Publications Ltd., Plymouth, 2009.
- [7] P. Dillmann, D. Watkinson, E. Angelini, A. Adriens, Corrosion and Conservation of Cultural Heritage Metallic Artefacts, Woodhead Publishing, Oxford, 2013.
- [8] H. Yoshikawa, E. Gunji, M. Tokuda, Long term stability of iron for more than 1500 years indicated by archeological samples from yamato 6th century, *J. Nucl. Mater.* 379 (2008) 112–117.
- [9] D. Feron, D.D. Macdonald, Prediction of long term corrosion behaviour in nuclear waste systems, in: EFC (Ed.) EFC Series, Maney, London, 2001, pp. 515.
- [10] D. Feron, D. Crusset, J.-M. Gras, D.D. Macdonald, Prediction of Long Term Corrosion Behaviour in Nuclear Waste Systems, ANDRA, Chatenay-Malabry, 2004.
- [11] D. Neff, P. Dillmann, L. Bellot-Gurlet, G. Beranger, Corrosion of iron archaeological artefacts in soil: characterisation of the corrosion system, *Corros. Sci.* 47 (2005) 515–535.
- [12] M. Saheb, Long-term anoxic corrosion of iron, in: P. Dillmann, D. Watkinson, E. Angelini, A. Adriens (Eds.), Corrosion and Conservation of Cultural Heritage Metallic Artefacts, Woodhead Publishing, Oxford, 2013, pp. 260–284.
- [13] M. Saheb, D. Neff, C. Bataillon, E. Foy, P. Dillmann, Copper tracing to determine the micrometric electronic properties of a thick ferrous corrosion layer formed in an anoxic medium, *Corros. Sci.* 53 (2011) 2201–2207.
- [14] M. Saheb, M. Descostes, D. Neff, H. Matthiesen, A. Michelin, P. Dillmann, Iron corrosion in an anoxic soil: comparison between thermodynamic modelling and ferrous archaeological artefacts characterised along with the local in situ geochemical conditions, *Appl. Geochem.* 25 (2010) 1937–1948.
- [15] A. Michelin, E. Drouet, E. Foy, J.J. Dynes, D. Neff, P. Dillmann, Investigation at the nanometre scale on the corrosion mechanisms of archaeological ferrous artefacts by STXM, *J. Anal. At. Spectrom.* 28 (2013) 59–66.
- [16] E.B. Castro, J.R. Vilche, A.J. Arvia, Iron dissolution and passivation in $\text{K}_2\text{CO}_3/\text{KHCO}_3$ solutions rotating ring disc electrode and XPS studies, *Corros. Sci.* 32 (1991) 37–50.
- [17] C.M. Rangel, I.T. Fonseca, R.A. Leitão, Some aspects of the electrochemical behaviour of mild steel in carbonate/bicarbonate solutions, *Electrochim. Acta* 31 (1986) 1659–1662.
- [18] C. Bataillon, C. Musy, M. Roy, Corrosion des surconteneurs de déchets, cas d'un surconteneur en acier faiblement allié, *J. Phys. IV France* (2001) 267–274.
- [19] J. Han, D. Young, H. Colijn, A. Tripathi, S. Nestic, Chemistry and structure of the passive film on mild steel in CO_2 corrosion environments, *Ind. Eng. Chem. Res.* 48 (2009) 6296–6302.
- [20] A.J. Davenport, L.J. Oblonsky, M.P. Ryan, M.F. Toney, The structure of the passive film that forms on iron in aqueous environments, *J. Electrochem. Soc.* 147 (2000) 2162–2173.
- [21] L.J. Oblonsky, M.P. Ryan, H.S. Isaacs, In situ XANES study of the formation and reduction of the passive film formed on Fe in acetate solution, *Corros. Sci.* 42 (2000) 229–241.
- [22] J.K. Heuer, J.F. Stubbs, An XPS characterization of FeCO_3 films from CO_2 corrosion, *Corros. Sci.* 41 (1999) 1231–1243.
- [23] C.T. Lee, M.S. Odziemkowski, D.W. Shoesmith, An in situ Raman-electrochemical investigation of carbon steel corrosion in $\text{Na}_2\text{CO}_3/\text{NaHCO}_3$, Na_2SO_4 and NaCl solutions, *J. Electrochem. Soc.* 153 (2006) B33–B41.
- [24] C.T. Lee, Z. Qin, M. Odziemkowski, D.W. Shoesmith, The influence of groundwater anions on the impedance behaviour of carbon steel corroding under anoxic conditions, *Electrochim. Acta* 51 (2006) 1558–1568.
- [25] R.N. Parkins, S. Zhou, The stress corrosion cracking of C–Mn steel in $\text{CO}_2/\text{HCO}_3^-/\text{CO}_3^{2-}$ solutions. II: Electrochemical and other data, *Corros. Sci.* 39 (1997) 175–191.
- [26] B.W.A. Sherar, P.G. Keech, Z. Qin, F. King, D.W. Shoesmith, Nominally anaerobic corrosion of carbon steel in near-neutral pH saline environments, *Corrosion* 66 (2010). 045001–045001–045011.
- [27] M. Saheb, D. Neff, P. Dillmann, H. Matthiesen, E. Foy, Long-term corrosion behaviour of low-carbon steel in anoxic environment: characterisation of archaeological artefacts, *J. Nucl. Mater.* 379 (2008) 118–123.
- [28] M. Saheb, D. Neff, P. Dillmann, H. Matthiesen, E. Foy, L. Bellot-Gurlet, Multisectional corrosion behaviour of low carbon steel in anoxic soils: characterisation of corrosion system on archaeological artefacts, *Mater. Corros.* 60 (2009) 99–105.
- [29] D. Neff, L. Bellot-Gurlet, P. Dillmann, S. Reguer, L. Legrand, Raman imaging of ancient rust scales on archaeological iron artefacts for long-term atmospheric corrosion mechanisms study, *J. Raman Spectrosc.* 37 (2006) 1228–1237.
- [30] M.C. Bernard, S. Duval, S. Joiret, M. Keddam, F. Ropital, H. Takenouti, Analysis of corrosion products beneath an epoxy-amine varnish film, *Prog. Org. Coat.* 45 (2002) 399–404.
- [31] S. Savoye, L. Legrand, G. Sagon, S. Lecomte, A. Chausse, R. Messina, P. Toulhoat, Experimental investigations on iron corrosion products formed in bicarbonate/carbonate-containing solutions at 90 °C, *Corros. Sci.* 43 (2001) 2049–2064.
- [32] L.J. Simpson, C.A. Melendres, Surface-enhanced Raman spectroelectrochemical studies of corrosion films on iron in aqueous carbonate solution, *J. Electrochem. Soc.* 143 (1996) 2146–2152.
- [33] M. Saheb, D. Neff, L. Bellot-Gurlet, P. Dillmann, Raman study of a deuterated iron hydroxycarbonate to assess long-term corrosion mechanisms in anoxic soils, *J. Raman Spectrosc.* 42 (2011) 1100–1108.
- [34] S.J. Oh, D.C. Cook, H.E. Townsend, Characterization of iron oxides commonly formed as corrosion products on steel, *Hyperfine Interact.* 112 (1998) 59–65.
- [35] N. Boucherit, P. Delichere, S. Joiret, A.H.-L. Goff, Passivity of iron alloys studied by voltammetry and Raman spectroscopy, *Mater. Sci. Forum* 44–45 (1989) 51–62.
- [36] D.L.A. De Faria, S.V. Silva, M.T.d. Oliveira, Raman microspectroscopy of some iron oxides and oxyhydroxides, *J. Raman Spectrosc.* 28 (1997) 873–878.
- [37] D. Thierry, D. Persson, C. Leygraf, N. Boucherit, A.H.-L. Goff, Raman spectroscopy and XPS investigations of anodic corrosion films formed on Fe–Mo alloys in alkaline solution, *Corros. Sci.* 32 (1991) 273–284.
- [38] D. Bersani, P.P. Lottici, A. Montenero, Micro-Raman investigation of iron oxide films and powders produced by sol–gel syntheses, *J. Raman Spectrosc.* 30 (1999) 355–360.

- [39] A. Demoulin, C. Trigance, D. Neff, E. Foy, P. Dillmann, V. L'Hostis, The evolution of the corrosion of iron in hydraulic binders analysed from 46- and 260-year-old buildings, *Corros. Sci.* 52 (2010) 3168–3179.
- [40] D.R.G. Mitchell, DiffTools: electron diffraction software tools for DigitalMicrograph™, *Microsc. Res. Tech.* 71 (2008) 588–593.
- [41] P.A. Fenter, M.L. Rivers, N.C. Sturchio, S.R. Sutton, Applications of Synchrotron Radiation in Low-Temperature Geochemistry and Environmental Science. *Reviews in Mineralogy & Geochemistry*, Geochemical Society and Mineralogical Society of America, Washington, DC, 2002.
- [42] J.J. Dynes, T. Tylliszczak, T. Araki, J.R. Lawrence, G.D.W. Swerhone, G.G. Leppard, A.P. Hitchcock, Speciation and quantitative mapping of metal species in microbial biofilms using scanning transmission X-ray microscopy, *Environ. Sci. Technol.* 40 (2006) 1556–1565.
- [43] K.V. Kaznatcheev, C. Karunakaran, U.D. Lanke, S.G. Urquhart, M. Obst, A.P. Hitchcock, Soft X-ray spectromicroscopy beamline at the CLS: commissioning results, *Nucl. Instrum. Methods Phys. Res., Sect. A* 582 (2007) 96–99.
- [44] J.A. Brandes, S. Wirick, C. Jacobsen, Carbon K-edge spectra of carbonate minerals, *J. Synchrotron Radiat.* 17 (2010) 676–682.
- [45] J. Stohr, *NEXAFS Spectroscopy*, Springer, New-York, 2003.
- [46] A.P. Hitchcock, aXis2000 is an IDL-Based Analytical Package Free for Noncommercial Use, <<http://unicorn.mcmaster.ca>>.
- [47] M. Saheb, P. Berger, L. Raimbault, D. Neff, P. Dillmann, Investigation of iron long-term corrosion mechanisms in anoxic media using deuterium tracing, *J. Nucl. Mater.* 423 (2012) 61–66.
- [48] M. Saheb, D. Neff, J. Demory, E. Foy, P. Dillmann, Characterisation of corrosion layers formed on ferrous artefacts buried in anoxic media, *Corros. Eng., Sci. Technol.* 45 (2010) 381–387.
- [49] M.F. Toney, A.J. Davenport, L.J. Oblonsky, M.P. Ryan, C.M. Vitus, Atomic structure of the passive oxide film formed on iron, *Phys. Rev. Lett.* 79 (1997) 4282–4285.
- [50] H.-H. Strehblow, V. Maurice, P. Marcus, Passivity of metals, in: P. Marcus (Ed.), *Corrosion Mechanisms in Theory and Practice*, Taylor and Francis, 2012, pp. 236–323.
- [51] H.D. Speckmann, M.M. Lohrengel, J.W. Schultze, H.H. Strehblow, The Growth and Reduction of Duplex Oxide Films on Copper, *Ber. Bunsenges. Phys. Chem.* 89 (1985) 392–402.
- [52] C. Bataillon, F. Bouchon, C. Chainais-Hillairet, C. Desgranges, E. Hoarau, F. Martin, S. Perrin, M. Tupin, J. Talandier, Corrosion modelling of iron based alloy in nuclear waste repository, *Electrochim. Acta* 55 (2010) 4451–4467.
- [53] D.C. Cook, Spectroscopic identification of protective and non-protective corrosion coatings on steel structures in marine environments, *Corros. Sci.* 47 (2005) 2550–2570.
- [54] M. Bouchar, E. Foy, D. Neff, P. Dillmann, The complex corrosion system of a medieval iron rebar from the Bourges' Cathedral. Characterization and reactivity studies, *Corros. Sci.* 76 (2013) 361–372.
- [55] J. Chivot, Thermodynamique des produits de corrosion: Fonctions thermodynamiques, diagrammes de solubilité, diagrammes E-pH des systèmes Fe–H₂O, Fe–CO₂–H₂O, Fe–S–H₂O, Cr–H₂O et Ni–H₂O en fonction de la température, ANDRA (2004).
- [56] T.R. Lee, R.T. Wilkin, Iron hydroxy carbonate formation in zerovalent iron permeable reactive barriers: characterization and evaluation of phase stability, *J. Contam. Hydrol.* 116 (2010) 47–57.
- [57] M. Saheb, Etude des mécanismes de corrosion à très long terme des objets ferreux en milieu anoxique: Apport des analogues archéologiques, Université Paris Est, 2009.
- [58] C. Rémazeilles, P. Refait, Fe(II) hydroxycarbonate Fe₂(OH)₂CO₃ (chukanovite) as iron corrosion product: synthesis and study by Fourier Transform Infrared Spectroscopy, *Polyhedron* 28 (2009) 749–756.
- [59] M.S. Odziemkowski, T.T. Schuhmacher, R.W. Gillham, E.J. Reardon, Mechanism of oxide film formation on iron in simulating groundwater solutions: Raman spectroscopic studies, *Corros. Sci.* 40 (1998) 371–389.
- [60] L.J. Oblonsky, A.J. Davenport, M.P. Ryan, H.S. Isaacs, R.C. Newman, In situ X-ray absorption near edge structure study of the potential dependence of the formation of the passive film on iron in borate buffer, *J. Electrochem. Soc.* 144 (1997) 2398–2404.
- [61] H. Matthiesen, D. Gregory, P. Jensen, B. Sørensen, Environmental monitoring at Nydam, a waterlogged site with weapon sacrifices from the Danish Iron age. I: A comparison of methods used and results from undisturbed conditions, *J. Wetland Archaeol.* 4 (2004) 55–74.